Revista Internacional de Métodos Numéricos para Cálculo y Diseño en Ingeniería

Tech Science Press

https://doi.org/10.32604/rimni.2026.080803

ARTICLE

A Numerical Modeling Framework for Hydraulic Performance Evaluation and Sensitivity Analysis of Underground Pump Station Schemes for Multistage Centrifugal Pumps

Yuan Tang[1], Tengjiao Guo[1], Ran Tao[1,2,*] and Ruofu Xiao[1,2]

[1]College of Water Resources and Intelligence Engineering, China Agricultural University, Beijing, China
[2]Beijing Engineering Research Center of Safety and Energy Saving Technology for Water Supply Network System, Beijing, China

*Corresponding Author: Ran Tao. Email: randytao@cau.edu.cn

Received: 14 February 2026; Accepted: 31 March 2026; Published: 06 November 2026

ABSTRACT: With the increasing application of pumping systems in energy and industrial fields, accurate hydraulic performance evaluation and parameter analysis have become essential for improving the design and operation reliability of pump stations. This study develops a CFD-based numerical modeling framework for the hydraulic assessment and sensitivity analysis of underground pump station schemes equipped with multistage centrifugal pumps. The Reynolds-averaged Navier–Stokes (RANS) approach combined with the RNG k-ε turbulence model was employed to establish three-dimensional numerical models of different centrifugal pump configurations. Based on the obtained numerical results, the hydraulic performance characteristics, internal flow behaviors, and engineering applicability of three pump schemes were systematically evaluated. Furthermore, a modified Morris screening method integrated with the Latin hypercube sampling–partial rank correlation coefficient (LHS–PRCC) method was incorporated into the numerical framework to quantify the influence of six hydraulic parameters on pump head and efficiency. The results demonstrate that the single-suction vertical three-stage volute centrifugal pump with conventional flow channels exhibits the best overall hydraulic adaptability for the investigated underground pump station. The impeller outlet width shows the highest sensitivity to pump head, whereas flow rate is the dominant factor affecting efficiency. The diffusion section height of the volute has a relatively limited influence on both head and efficiency. The proposed numerical framework provides a systematic methodology for integrating CFD simulation and parameter sensitivity analysis, offering quantitative guidance for the hydraulic performance evaluation and design of underground pump station systems.

KEYWORDS: Numerical modeling framework; multistage centrifugal pump; CFD; sensitivity analysis; hydraulic performance; flow channel design

1 Introduction

The water intake pump station is an important component of the urban water supply system. It plays a crucial role in the fields of production water use and cross-basin water transfer. The design of large-scale water intake pump stations mainly selects appropriate water intake pump types based on the water source situation. The corresponding pump rooms and ancillary facilities are designed according to the pump types. The reasonable selection of pump type is very important for the reliability and safety of water supply in a large area. In recent years, many scholars have studied the influence of geometric parameters on the hydraulic performance of centrifugal pumps. For example, Sonawat et al. [1] and Jiang et al. [2] discussed

Copyright © 2027 The Authors. Published by Tech Science Press. This work is licensed under a Creative Commons Attribution 4.0 International License, which permits unrestricted use, distribution, and reproduction in any medium, provided the original work is properly cited.

the role of impeller geometric parameters, and found that among the multiple geometric parameters, the clearance between impeller and rotor-stator and the staggered angle of impeller had the most significant impact on impeller vibration. Wang et al. [3] analyzed the influence of flow and speed on the pressure pulsation of double—suction centrifugal pump through experiments. Dehghan and Shojaeefard [4] studied the influence of centrifugal pump volute on head and hydraulic efficiency at the optimal efficiency point by using experimental and numerical simulation methods. At the same time, a standard to measure the pump performance loss at the beginning of cavitation was also defined [5]. Chang et al. [6] assess the impact of wall roughness on energy dissipation mechanisms through entropy production analysis. With the rapid development of computational fluid dynamics (CFD) technology, many researchers have also begun to study how to use reliable turbulence models and accurate numerical methods to predict complex flow phenomena in centrifugal pumps [7–11]. Gonzalez et al. [12] compared the results of numerical simulations and experiments to verify the effectiveness of CFD methods in capturing pressure pulsations inside centrifugal pumps. Alemi et al. [13] simulated a rectangular volute pump using three different turbulence models. The study showed that compared to the rectangular cross-sectional volute, the minimum radial force of the circular volute geometry occurs at higher flow velocity positions. Lettieri et al. [14] systematically analyzed the impact of geometric shape changes on pump stability and performance. The research has found that unsteady flow separation in the reflux channel will cause changes in the incident angle on the volute tongue. Bozorgasareh et al. [15] investigated the effect of a new impeller shroud on the pressure head and efficiency of a semi—open centrifugal pump using experimental and numerical methods. The study showed that the new impeller design significantly improved the pressure head and efficiency of the semi-open centrifugal pump. Gu et al. [16] studied the effect of axial oscillation frequency of the new multi-stage centrifugal pump floating impeller on pump pressure fluctuations using dynamic grids. The research results indicate that efficiency and head all exhibit periodic variations related to the oscillation frequency of the impeller. In addition, the non-dominated sorting genetic algorithms were used to carry out multi-objective optimization of the impeller [17–20]. These studies show that the algorithm has good performance under multiple optimization objectives and can effectively balance various indicators, so as to improve the overall performance of the impeller. Compared with the original model, the flow in the optimized impeller area has become more stable. Li et al. [21] concluded through the combination of experimental analysis and numerical simulation that slight blade breakage has the least impact on pump head and efficiency, while severe blade breakage leads to a significant decrease in head and relatively stable efficiency.

Sensitivity analysis enables us to evaluate the sensitivity of the optimization model to the input uncertainty, so as to provide a more solid basis for decision makers [22,23]. With the in-depth study, the sensitivity analysis method has made significant progress and has been widely used in the field of hydraulic engineering. These methods provide an important quantitative basis for engineering design and decision-making, and can help identify key factors and optimize system performance. Yi et al. [24] conducted a sensitivity analysis on the water quality model using Morris and further identified and analyzed the model parameters for uncertainty. Xu et al. [25] proposed using the LH-OAT method to analyze the sensitivity of the SWAP-EPIC model. However, sensitivity analysis is less commonly used in screening design parameters that can affect the performance and efficiency of centrifugal pumps. Stübing et al. [26] designed and optimized the impeller of a centrifugal pump using ANSYS CFX and the ANSYS OptisLang module. This will maximize hydraulic efficiency and reduce torque. At present, there is no comprehensive study on the use of the Morris screening method and the LHS-PRCC sensitivity analysis method for multi-stage centrifugal pumps. Chang et al. [27] proposed to use the PB-WLHS method to obtain the influence of fluidic oscillator nozzle parameters on hydraulic performance and the optimal geometric configuration.

In this study, a CFD-based numerical modeling framework integrating hydraulic performance evaluation and sensitivity analysis was developed for the design assessment of underground pump station schemes equipped with multistage centrifugal pumps. Taking an underground pumping station of a water source project as an engineering case, three centrifugal pump configurations, including two single-suction vertical three-stage centrifugal pumps and one double-suction centrifugal pump, were investigated based on their geometric characteristics and hydraulic performance. The three-dimensional numerical models were established using the Reynolds-averaged Navier–Stokes approach with the RNG k-ε turbulence model. Furthermore, the modified Morris screening method and the LHS–PRCC method were integrated into the proposed framework to quantify the effects of representative hydraulic parameters on pump head and efficiency. This approach provides a systematic numerical methodology for identifying the dominant parameters and evaluating their contributions to centrifugal pump performance.

The structure of this article is as follows: Section 2 introduces the research case and the main parameters of the centrifugal pump. In Section 3, we provided a detailed introduction to two sensitivity analysis methods as well as the RNG k-ε turbulence model. In Section 4, we provided a detailed introduction to the relevant steps of numerical simulation and the reliability verification of numerical calculations. In Section 5, the advantages and disadvantages of three schemes and the calculation results of two sensitivity analyses were compared and analyzed. Finally, the conclusions of this study were presented in Section 6.

2 Main Pump Parameters

The pump model planned to be used in the underground pumping station is a vertical single-suction three-stage centrifugal pump. To reduce computational resources, the model pump is used in numerical simulation. The model of single suction three-stage centrifugal pump is shown in Fig. 1. The model is similar to the prototype from the inlet of the inlet pipe to the outlet of the snail shell. The scale factor between the prototype and the model is 4.01. The rotation direction of the model pump is clockwise. The design flow rate of the pump is 0.19 m^3/s, the rated head is 108.7 m, and the rated speed is 1220 r/min. The number of blades per stage of the impeller is 9 sets, and the number of guide vanes is 13 sets. The working parameters of the model pump under 0.7~1.4 Q operating conditions are shown in Table 1.

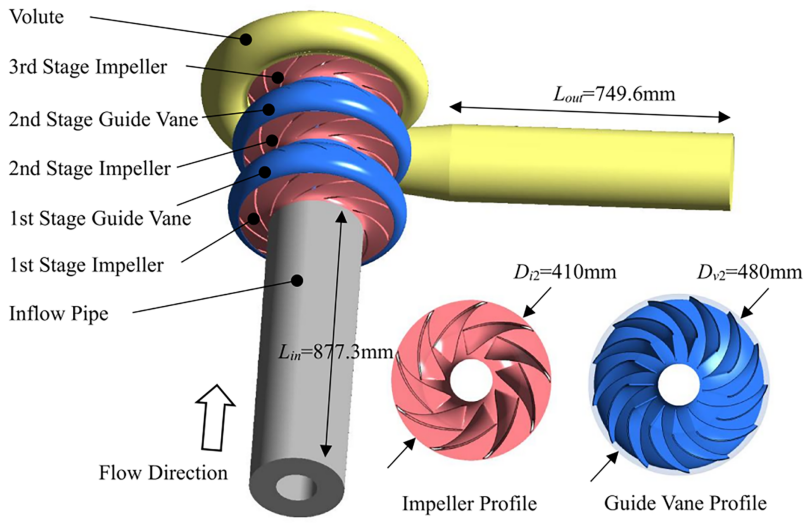


Figure 1: Three stage centrifugal pump model.

Table 1: Model pump working parameters.

Working Condition	Flow Rate (m^3/s)	Head (m)	Efficiency (%)
0.7 Q	0.133	116.22	69.514
0.8 Q	0.152	113.68	73.501
0.9 Q	0.171	112.86	78.362
1.0 Q	0.190	108.94	80.616
1.1 Q	0.209	103.26	81.453
1.2 Q	0.228	98.366	81.164
1.3 Q	0.247	92.189	79.543
1.4 Q	0.266	85.217	77.03

Similar to the prototype pump, the traditional flow channel has been replaced with a new design with equally wide flow channels and guide vanes, as shown in Fig. 2a,b. Based on the impeller model of single stage centrifugal pump, the double suction centrifugal pump impeller model is established through operations such as mirroring, rotation, merging, and fluid extraction, as shown in Fig. 2c. The single suction vertical three-stage pump with traditional flow channel is named as pump 1, the single suction vertical three-stage pump with new flow channel is named as pump 2, and the single-stage double suction centrifugal pump is named as pump 3. The main design parameters of each centrifugal pump are shown in Table 2. The difference between pump 1 and pump 2 lies in the shape and size of the flow channel, as shown in Fig. 2.

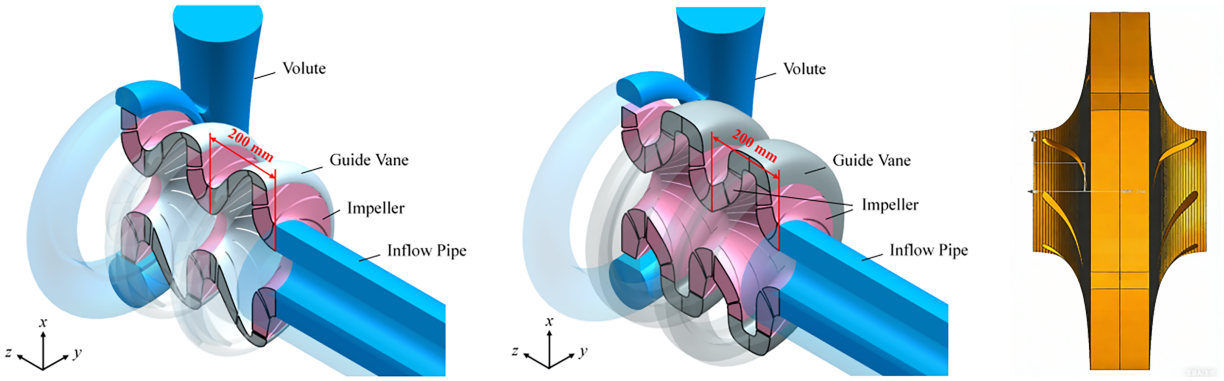


Figure 2: Centrifugal pump model: (**a**) Traditional channel design (Pump 1); (**b**) New channel design (Pump 2); (**c**) Double suction centrifugal pump impeller model (Pump 3).

Table 2: Main design parameters of each centrifugal pump.

Centrifugal Pump	Number of Impeller Blades	Rotational Speed (r/min)	Head/m	Specific Speed	Hub Diameter/ mm	Suction Diameter/ mm	Impeller Diameter/ mm	Outlet Width/ mm
Pump 1	9/9/9	1220	108.7	131.43	110	255	410	45
Pump 2	9/9/9	1220	108.7	131.43	110	255	410	45
Pump 3	6	1220	108.7	40.77	80	230	686	62

To reduce the influence of geometric scale and operating conditions, dimensionless performance parameters have been introduced, including the flow coefficient ϕ.

The flow coefficient equation for ϕ is:

$$\phi = \frac{Q}{nD^3} \tag{1}$$

Since Pumps 1 and 2 are multistage pumps while Pump 3 is single-stage, the head coefficient ψ is expressed as follows:

$$\psi = \frac{gH}{n^2D^2} \tag{2}$$

3 Models and Methods

3.1 Governing Equation and Cavitation Model

This numerical simulation is based on the full cavitation model developed by Singhal et al. [28]. Without considering the heat generated by internal friction and the heat transfer between the pump and the outside world, the basic integral equations for the conservation of mass and momentum of the two-phase mixture of air and water are as follows:

$$\frac{\partial}{\partial \mathrm{t}} \int_{\Omega(t)} \rho \mathrm{d}\Omega + \int_{\sigma} \rho \left(v - v_{\sigma}\right) \cdot n \mathrm{d}\sigma = 0 \tag{3}$$

$$\frac{\partial}{\partial t} \int_{\Omega(\mathrm{t})} \rho v d\Omega + \int_{\sigma} \rho \left[\left(v - v_{\sigma}\right) \cdot n\right] v d\sigma = \int_{\sigma} \tilde{\tau} \cdot n d\sigma - \int_{\sigma} p n d\sigma + \int_{\Omega} f d\Omega \tag{4}$$

The cavitation model is a key physical model for studying the fluid phase transition process under pressure changes. The cavitation model uses the following formula to describe steam distribution:

$$\frac{\partial}{\partial \mathrm{t}} \int_{\Omega(t)} \rho \mathrm{d}\Omega + \int_{\sigma} \rho \left[\left(v - v_{\sigma}\right) \cdot n\right] f \mathrm{d}\sigma = \int_{\sigma} \left(D_f + \frac{\mu_t}{\sigma_t}\right) \left(\nabla f \cdot n\right) \mathrm{d}_{\sigma} + \int_{\sigma} \left(\mathrm{R}_e - \mathrm{R}_c\right) \mathrm{d}\Omega \tag{5}$$

The uniqueness of this full cavitation model lies in its excellent convergence. Compared with other cavitation models, this model contains not only the vaporization pressure of liquid, but also the physical parameters such as liquid surface tension and non-condensable gas concentration, which may be more suitable for studying and calculating the cavitation flow of liquid. In addition, this cavitation model can not only accurately predict the impact of cavitation on efficiency, but also accurately predict the possible location of cavitation damage.

In order to facilitate readers to understand the fluid cavitation state reasonably, the dimensionless parameter of cavitation number is generally used for classification. The smaller the cavitation number σ, the more prone cavitation is to occur. The formula of cavitation number σ is as follows:

$$\sigma = \left(p_{\infty} - p_{\mathrm{v}}\right) / \left(0.5 \rho_l {u_i}^2\right) \tag{6}$$

where p_{∞} is the outlet pressure of the fluid domain, Pa; p_{v} is the vapor pressure of water at 25°C, Pa; ρ_l is the density of the liquid, kg/m^3; and u_i is the incoming flow velocity, m/s.

3.2 RNG k-ε Model

The standard k-ε equation may cause distortion when used for strong eddies or curved walls. The viscosity term is subjected to large-scale motion and correction to remove small-scale effects from the control equation. The resulting equation is called the RNG k-ε equation.

The transportation equation for $\boldsymbol{k}$ is:

$$\frac{\partial(\rho k)}{\partial t}+\frac{\partial(\rho k u_i)}{\partial x_i}=\frac{\partial}{\partial x_j}\left[\alpha_k \mu_{eff}\frac{\partial k}{\partial x_j}\right]+G_k+\rho\varepsilon \tag{7}$$

The transportation equation for $\boldsymbol{\varepsilon}$ is:

$$\frac{\partial(\rho \varepsilon)}{\partial t}+\frac{\partial(\rho \varepsilon u_i)}{\partial x_i}=\frac{\partial}{\partial x_j}\left[\alpha_\varepsilon \mu_{eff}\frac{\partial \varepsilon}{\partial x_j}\right]+\frac{C_{1\varepsilon}^{*}\varepsilon}{k}G_k-C_{2\varepsilon}\rho\frac{\varepsilon^2}{k} \tag{8}$$

Compared with the standard k-ε model, the RNG k-ε model can better simulate flows with high strain rates and significant streamline curvature. In addition, the model considers the rotation effect, thus improving the accuracy of calculations for strong rotating flows. Two models are provided for users to choose from for calculating the three-dimensional flow field of pumps. These two are the standard k-ε model and the RNG k-ε model, respectively. Choose the RNG k-ε model with better performance here.

3.3 Revised Morris Screening Method

Morris sensitivity analysis can reflect the changes in calculation results under subtle changes in influencing factors [29,30]. The guiding principle of the Morris method is to determine which factors can be considered influential. The Morris screening method is established on the basis of the key influencing factors, in which the influence measure of the i-th factor is usually given by:

$$e_i=\frac{y(x_1,x_2,x_3,\ldots,x_i+\Delta,\ldots,x_n)-y(x_1,x_2,x_3,\ldots,x_i,x_n)}{\Delta} \tag{9}$$

The sensitivity coefficient S of the modified Morris screening method is taken as the average of multiple calculated values:

$$S=\sum_{i=0}^{n-1}\frac{(y_{i+1}-y_i)/y_0}{(P_{i+1}-P_i)/100}/(n-1) \tag{10}$$

3.4 LHS-PRCC

The partial rank correlation coefficient method (PRCC) based on Latin hypercube sampling (LHS) provides an effective means to evaluate the sensitivity of output variables to the changes of input parameters [31]. Its main advantage is that it can achieve the same accuracy as simple random sampling with less samples, and it performs better than random sampling in estimating the mean and population distribution function. In the LHS method, the range of parameters is divided into N equal probability intervals, and sample points are randomly selected from each interval [32]. The specific steps of LHS include: evenly dividing the input range of each parameter into N parts, randomly selecting representative parameters in each partition, and finally combining the selected parameters into sampling results.

The Partial correlation coefficient (PCC) analysis is mainly used to exclude the impact of other variables on the results under the interaction of multiple factors [33]. The accuracy of this analysis method depends

on the number of variables involved in the study. The correlation $r_{x_j,y}$ between the input variable x_j and the output result y for a series of observations $\left(x_{ij}, y_i\right)$ is defined by the following equation:

$$r_{x_j,y} = \frac{\sum_{i=1}^{N}\left(x_{ij}-\overline{x}_j\right)\left(y_i-\overline{y}\right)}{\left[\sum_{i=1}^{N}\left(x_{ij}-\overline{x}_j\right)^2\right]^{1/2}\left[\sum_{i=1}^{N}\left(y_i-\overline{y}\right)^2\right]^{1/2}} \tag{11}$$

$$\overline{y} = \sum_i y_i/N \tag{12}$$

$$\overline{x_j} = \sum_i x_{ij}/N \tag{13}$$

The partial correlation coefficient between the output variable y and the input variable x_j is obtained through the use of a series of regression models. The following two regression models are constructed:

$$\hat{Y} = b_0 + \sum_{k\neq j} b_k x_k \tag{14}$$

$$\hat{X}_j = c_0 + \sum_{k\neq j} c_k x_k \tag{15}$$

After adjusting for the linear effects of other variables in the analysis, the partial correlation coefficient provides a measure of the strength of the linear relationship between two variables.

4 Numerical Simulation

4.1 Numerical Calculation Settings

Mesh generation has always been one of the necessary steps in numerical simulation. The quality and quantity of meshes determine the convergence of numerical simulation. The grid partitioning process uses the software's unique Cartesian grid. The internal flow of the water pump is calculated through steady-state numerical simulation. The turbulence model adopts RNG k-ε turbulence model. The inlet boundary adopts the total pressure inlet, the outlet boundary adopts the static pressure outlet, and the pressure is set to 0 Pa. All solid walls are treated as non-slip walls. To ensure convergence, the residual is set to 10^{-4} and the number of steps is set to 500 in steady-state calculations. In the numerical simulations, the outlet boundary condition with a specified static pressure of 0 Pa corresponds to the gauge pressure, which means that the outlet pressure is referenced to the atmospheric pressure. The pump head is calculated based on the difference between the total pressure at the outlet and inlet sections. The hydraulic efficiency is obtained from the ratio between hydraulic power and shaft power. The shaft power is determined by integrating the torque acting on the rotating impeller surfaces and multiplying it by the angular velocity.

4.2 Reliability Verification of Numerical Calculations

Due to the significant impact of grid partitioning methods and numbers on the accuracy and computational resource consumption of numerical simulations, the GCI criterion based on Richardson extrapolation method was used to check the convergence of the grid [34,35]. The coarse grid N_1, medium grid N_2 and fine grid N_3 are used for sensitivity analysis. The parameters evaluated are Head $\boldsymbol{H}$and Efficiency $\boldsymbol{\eta}$. The calculation results are shown in Fig. 3 and Table 3. The results show that in the three grid thickness schemes, the GCI range is within the 5% threshold recommended in the reference, so the three schemes meet the engineering accuracy requirements. Finally, the medium number grid scheme is selected for numerical simulation, which takes into account the calculation cost and accuracy requirements. The final grid partitioning situation was determined while ensuring grid independence, as shown in Table 4. It should

be noted that each grid cell is derived from regular polyhedral grids generated by orthogonalization methods. The grid quality is very high, and there is no need to check the grid quality separately.

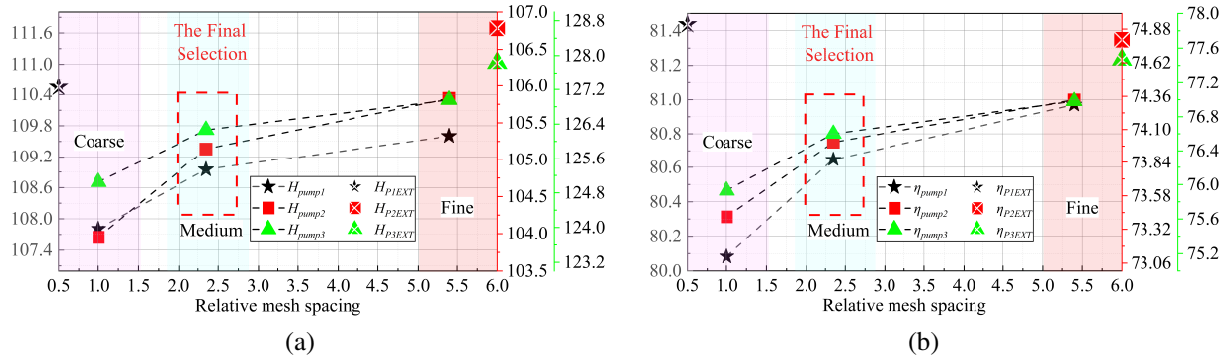


Figure 3: Grid dependence check: (**a**) Head H; (**b**) Efficiency η.

Table 3: Evaluation results of discretization error.

Parameter	H_{pump1}	η_{pump1}	H_{pump2}	η_{pump2}	H_{pump3}	η_{pump3}
N_1	704,584		894,407		167,001	
N_2	1,652,251		2,108,030		393,521	
N_3	3,791,916		4,905,175		942,671	
φ_1	107.806	80.083	103.952	73.417	125.050	75.930
φ_2	108.95	80.648	105.148	74	126.265	76.6
φ_3	109.604	80.971	105.831	74.333	126.959	76.983
ε^{21}	−0.654	−0.323	−0.683	−0.333	−0.694	−0.383
ε^{32}	−1.144	−0.565	−1.196	−0.583	−1.215	−0.67
$\phi^{21}{}_{ext}$	110.5486	81.4375	106.7833	74.7975	127.8318	77.4656
$e_a{}^{21}$ (%)	1.05	0.40	3.30	0.45	0.55	0.5
$e_{ext}{}^{21}$ (%)	1.45	0.57	0.89	0.62	0.68	0.62
$GCI_{fine}{}^{21}$ (%)	1.83	0.72	1.12	0.781	0.86	0.784

Table 4: Model pump grid division situation.

Centrifugal Pump	Number of Cells	Number of Faces	Number of Nodes
Pump 1	1,652,251	6,006,846	2,420,483
Pump 2	2,108,030	7,737,644	3,151,263
Pump 3	393,521	1,382,771	551,308

5 Result Analysis

5.1 CFD Result Analysis

The layout of centrifugal pump channel has a great influence on the flow field inside the volute, which changes the pressure and velocity distribution in the pump. As shown in Figs. 4 and 5, different pump designs have different effects on pressure gradient, velocity field and cavitation performance. Table 5 summarizes the calculation results of relevant parameters obtained through numerical simulation.

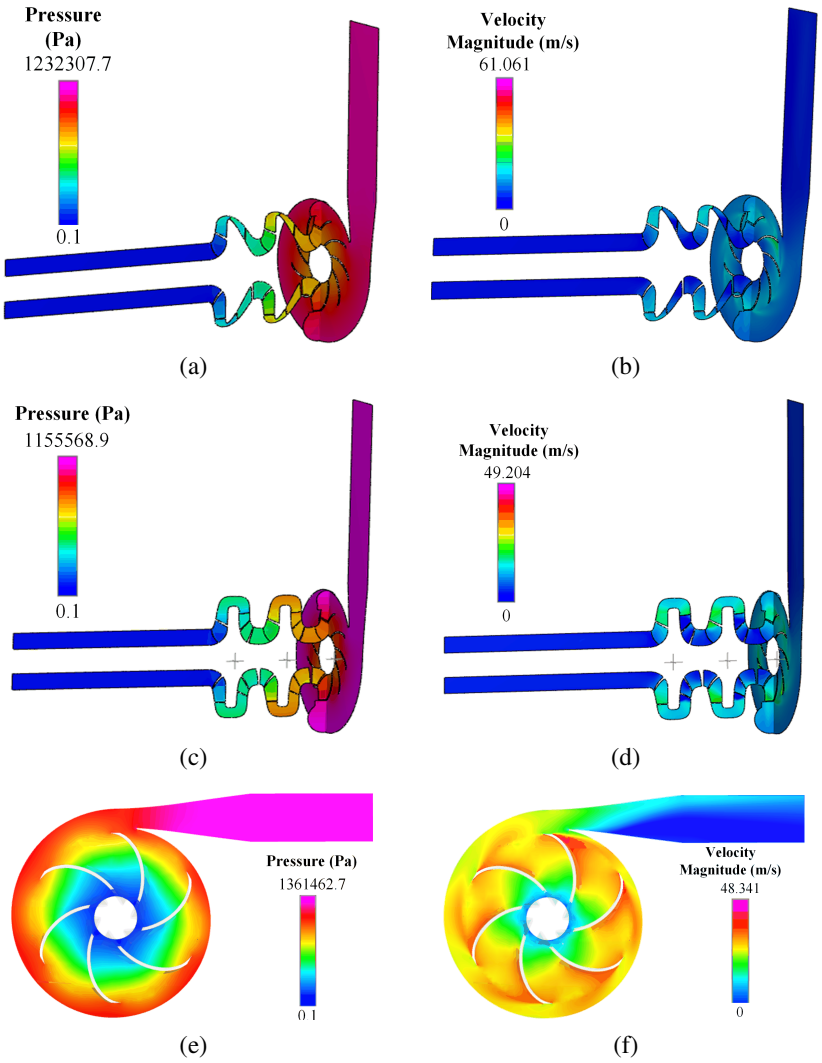


Figure 4: Pressure gradient distribution and velocity distribution: (**a**) Pressure gradient distribution of pump 1; (**b**) Velocity distribution of pump 1; (**c**) Pressure gradient distribution of pump 2; (**d**) Velocity distribution of pump 2; (**e**) Pressure gradient distribution of pump 3; (**f**) Velocity distribution of pump 3.

Fig. 4 shows the pressure gradient distribution and velocity distribution of different pump types. It can be seen from Fig. 4a,c that the pressure and velocity distribution in the suction chamber change significantly when located at different positions in the pump flow channel. As shown in Fig. 4b,d the liquid flow velocity near the first-stage impeller is relatively low, resulting in a corresponding decrease in pressure. The liquid in the second stage impeller has significantly larger high-pressure area compared to the liquid in the first stage impeller, and the liquid in the third stage impeller has larger high-pressure area compared to the liquid in the second stage impeller. The guide vanes between each stage of the impeller convert a portion of the kinetic energy of the liquid into potential energy, allowing the liquid to flow into the impeller at lower velocity. As shown in Fig. 4e,f, the pressure gradient distribution is uniform, and the pressure gradually increases from the inlet to the volute. The water flow velocity in the internal area of the impeller and some areas of the volute exceeds 48 m/s. According to the existing operating experience of the pumping station, when the sediment content in the water is high, the parts of the pump with a relative velocity greater than 31 m/s should be sprayed with anti-sediment wear coating.

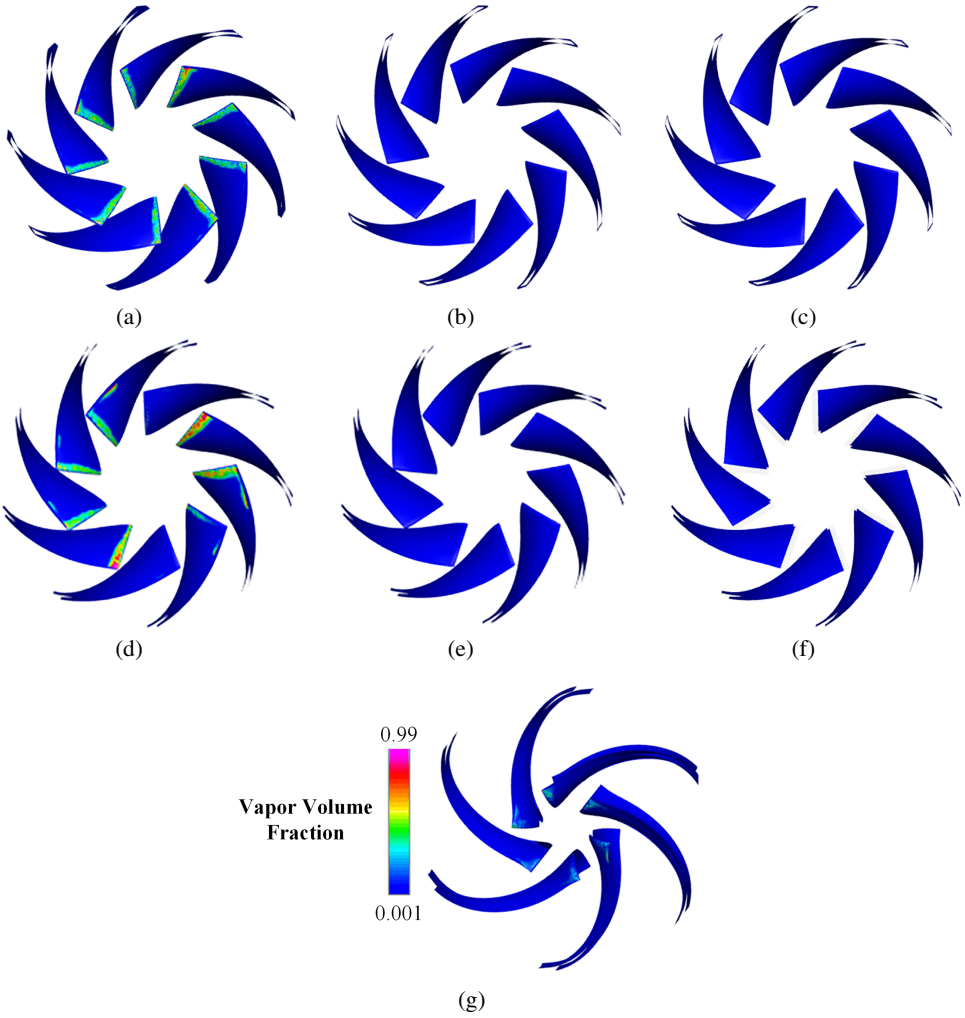


Figure 5: Distribution diagram of impeller air bubbles: (**a**) 1st stage blade of pump 1; (**b**) 2nd stage blade of pump 1; (**c**) 3rd stage blade of pump 1; (**d**) 1st stage blade of pump 2; (**e**) 2nd stage blade of pump 2; (**f**) 3rd stage blade of pump 2; (**g**) blade of pump 3.

Table 5: Pump performance parameter.

Output Parameters	Pump 1	Pump 2	Pump 3
Head/m	108.95	105.148	126.265
Efficiency/%	80.648	74	76.6
Flow coefficient ϕ	0.136	0.136	0.029
Head coefficient ψ	15.378	14.842	6.366
Cavitation number σ	11.548	10.827	12.761

In order to better understand the influence of different pump types on the development of cavitation and air bubbles inside the pump, as shown in Fig. 5, the distribution of air bubbles inside impellers of different numbers under rated conditions was taken. From Fig. 5a,d,g, it can be seen that the cavitation development process of impellers in different types of pumps is consistent. Bubbles initially form at the rear of the blade near the cover plate. As the inlet pressure decreases, the number of bubbles gradually increases along the

blade's working surface and at the impeller inlet. The area covered by the bubbles expands from the blade tip toward the middle and spreads further along the flow channel. As shown in Fig. 5b,c,e,f, the cavitation degree of the second and third stage blades of the multi-stage pump is relatively low. According to the data in Table 5, it can be seen that the impact of pump type on head and efficiency is very significant. Pump 3 provides high lift, but low efficiency; Pump 1, on the other hand, shows the best efficiency and is suitable for applications requiring high efficiency. Furthermore, the results of flow coefficient and head coefficient show that although pump 3 can provide high head, its flow characteristics and head coefficient are relatively low, which may make it show different performance in specific applications. In contrast, pump 1 have better comprehensive performance in efficiency and flow, especially suitable for occasions with high efficiency requirements. The cavitation number of pump 1 is less than that of pump 3 but much greater than that of pump 2. This indicates that pump 1 has a higher margin before cavitation, so that it can operate under a wider range of conditions without cavitation risk. Therefore, these results show that it is very important to select the appropriate type of pump for different engineering needs, especially when the head and efficiency need to be balanced, the efficiency advantage of pump 1 may be more prominent. In summary, based on the manufacturing and application of large vertical single-stage and multi-stage centrifugal pumps at home and abroad, the pump station adopts single suction vertical three-stage volute centrifugal pump (pump 1) with traditional flow channels. This will provide excellent technical support for engineering construction.

5.2 Sensitivity Analysis

5.2.1 Parameter Selection

Take the Head $\boldsymbol{H}$ and Efficiency $\boldsymbol{\eta}$ of the single suction vertical three-stage centrifugal pump as output parameters, and take the number of impeller blades $\boldsymbol{P}$, blade wrap angle $\boldsymbol{\Delta\varphi}$, blade angle at trailing edge $\boldsymbol{\beta}$, impeller outlet width $\boldsymbol{b}$, height of volute diffusion section $\boldsymbol{k}$ and flow rate $\boldsymbol{Q}$ as input parameters. For the convenience of expression, the unit of the number of impeller blades is set to pieces; The unit of the blade wrap angle is set to degree; The unit of the blade angle at trailing edge is set to degree; The unit of the impeller outlet width is set to mm; The unit of the height of volute diffusion section is set to millimeters; The unit of the flow rate is set to kilograms per second. The benchmark values and variation ranges of each parameter are shown in Table 6.

Table 6: Parameter benchmark values and their ranges.

Parameter Number	Parameter	Reference Value	Range
1	Number of impeller blades $\boldsymbol{P}$	27	23~31
2	Blade wrap angle $\boldsymbol{\Delta\varphi}$	60	51~69
3	Blade angle at trailing edge $\boldsymbol{\beta}$	27	23~31.1
4	Impeller outlet width $\boldsymbol{b}$	45	38.25~51.75
5	Height of volute diffusion section $\boldsymbol{k}$	330	280.5~379.5
6	Flow rate $\boldsymbol{Q}$	190	161.5~218.5

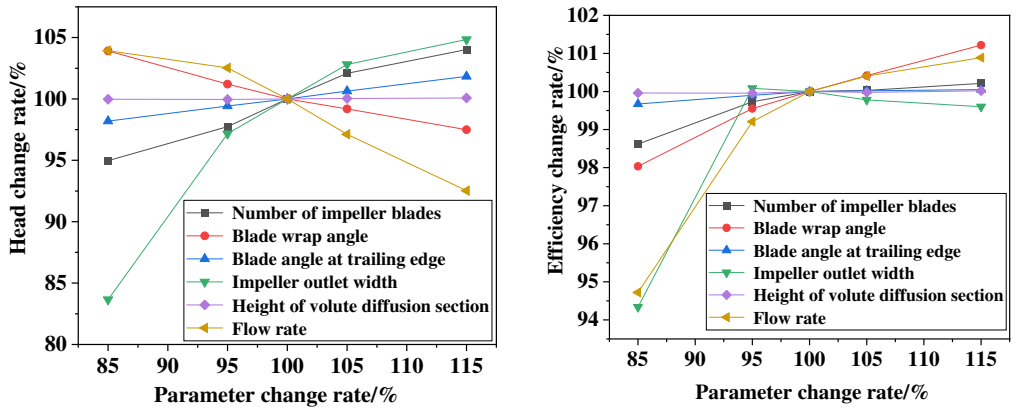
5.2.2 Morris Screening Method Results

The perturbation values of the parameters in this study are 85%, 95%, 105%, and 115% of the baseline values, while the remaining parameters remain fixed and unchanged. The head and efficiency corresponding to each parameter under different variation amplitudes are simulated and recorded. The simulated values are shown in Table 7.

Table 7: Simulation results of various parameters.

Number of Impeller Blades			Blade Wrap Angle			Blade Angle at Trailing Edge		
Input Parameter	Output Parameters		Input Parameter	Output Parameters		Input Parameter	Output Parameters	
	H (m)	η (%)		H (m)	η (%)		H (m)	η (%)
23	103.47	79.534	51	113.21	79.062	23	106.98	80.383
25	106.49	80.43	57	110.26	80.286	25.7	108.32	80.567
27	108.95	80.648	60	108.95	80.648	27	108.95	80.648
29	111.22	80.671	63	108.07	80.984	28.4	109.64	80.663
31	113.33	80.82	69	106.22	81.631	31.1	110.95	80.687
Impeller Outlet Width			**Height of Volute Diffusion Section**			**Flow Rate**		
Input Parameter	Output Parameters		Input Parameter	Output Parameters		Input Parameter	Output Parameters	
	H (m)	η (%)		H (m)	η (%)		H (m)	η (%)
38.25	91.148	76.081	280.5	108.92	80.617	0.1615	113.23	76.391
42.75	105.86	80.715	313.5	108.91	80.612	0.1805	111.7	80.008
45	108.95	80.648	330	108.95	80.648	0.190	108.95	80.648
47.25	112.01	80.47	346.5	108.99	80.629	0.1995	105.81	80.974
51.75	114.22	80.325	379.5	109.03	80.663	0.2185	100.81	81.365

Both the input and output results are expressed in terms of the form of rate of change, as shown in Fig. 6. From the figure, it is evident that the three parameters of the impeller outlet width $\boldsymbol{b}$, the number of impeller blades $\boldsymbol{P}$ and the blade angle at trailing edge $\boldsymbol{\beta}$ are positively correlated with the Head $\boldsymbol{H}$. The height of volute diffusion section $\boldsymbol{k}$ has no significant positive or negative correlation with the Head $\boldsymbol{H}$, while the two parameters of the blade wrap angle $\boldsymbol{\Delta\varphi}$ and flow rate $\boldsymbol{Q}$ are negatively correlated with the Head $\boldsymbol{H}$; The three parameters of the flow rate $\boldsymbol{Q}$, the blade wrap angle $\boldsymbol{\Delta\varphi}$ and the number of impeller blades $\boldsymbol{P}$ are positively correlated with the Efficiency $\boldsymbol{\eta}$, while the impeller outlet width $\boldsymbol{b}$ and blade angle at trailing edge $\boldsymbol{\beta}$ have no significant positive or negative correlation on Efficiency $\boldsymbol{\eta}$. The height of volute diffusion section $\boldsymbol{k}$ is negatively correlated with Efficiency $\boldsymbol{\eta}$.



(a)Head $\boldsymbol{H}$ (b)Efficiency $\boldsymbol{\eta}$

Figure 6: Curve of head and efficiency change rate vs. variation law of various parameters.

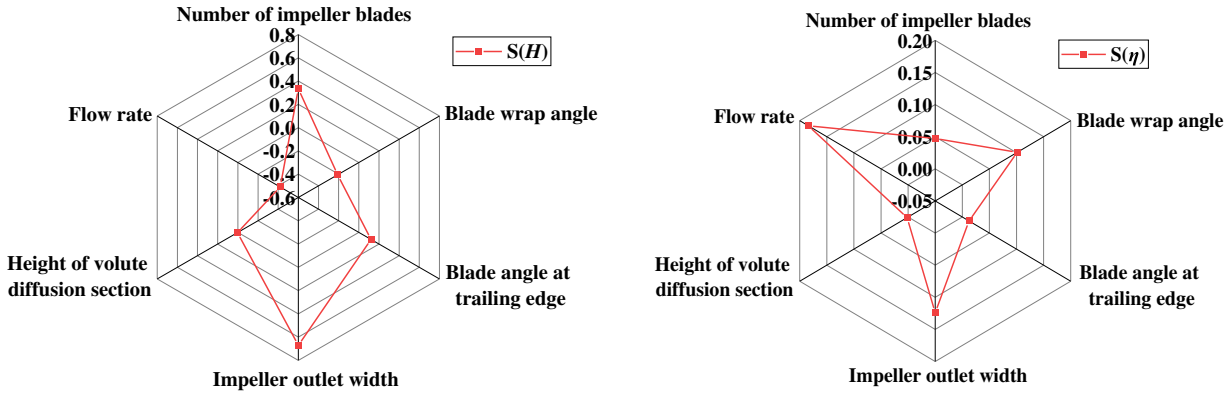
The calculation results in Table 7 are substituted into Eqs. (6) and (7) to obtain the sensitivity coefficients S of each parameter, and the sensitivity parameter is determined based on its absolute value. The calculation results are shown in Tables 8 and 9, and Fig. 7. The sensitivity of each parameter to Head H in descending order is as follows: $b > Q > P > \Delta\varphi > \beta > k$. The impeller outlet width b, the flow rate Q, the number of impeller blades P and the blade wrap angle $\Delta\varphi$ are sensitive parameters. The blade angle at trailing edge β is a medium sensitive parameter, and the height of volute diffusion section k is an insensitive parameter. The sensitivity of each parameter to Efficiency η in descending order is as follows: $Q > b > \Delta\varphi > P > \beta > k$. Among them, the flow rate Q, the impeller outlet width b and the blade wrap angle $\Delta\varphi$ are medium sensitive parameters, while the number of impeller blades P, the blade angle at trailing edge β and the height of volute diffusion section k are insensitive parameters.

Table 8: The sensitivity coefficient and the corresponding sensitivity level of each parameter in relation to the Head H.

Parameter Number	Parameter	S	Sensitivity Level
1	Number of impeller blades P	0.3348	Sensitivity parameter
2	Blade wrap angle $\Delta\varphi$	−0.2107	Sensitivity parameter
3	Blade angle at trailing edge β	0.1214	Medium sensitivity
4	Impeller outlet width b	0.6705	Sensitivity parameter
5	Height of volute diffusion section k	0.0044	Not sensitive
6	Flow rate Q	−0.4202	Sensitivity parameter

Table 9: The sensitivity coefficient and the corresponding sensitivity level of each parameter in relation to the Efficiency η.

Parameter Number	Parameter	S	Sensitivity Level
1	Number of impeller blades P	0.0473	Not sensitive
2	Blade wrap angle $\Delta\varphi$	0.1013	Medium sensitivity
3	Blade angle at trailing edge β	0.0124	Not sensitive
4	Impeller outlet width b	0.1239	Medium sensitivity
5	Height of volute diffusion section k	0.00195	Not sensitive
6	Flow rate Q	0.1841	Medium sensitivity



(a) Head H (b) Efficiency η

Figure 7: Sensitivity parameter S radar chart.

The above sensitivity ranking can be explained from the hydraulic roles of the selected parameters. Among all variables, the impeller outlet width $\boldsymbol{b}$ has the strongest influence on the Head $\boldsymbol{H}$ because it directly changes the flow area at the impeller outlet and thereby alters the outlet velocity distribution, flow diffusion process, and energy conversion capability inside the impeller-volute system. A larger outlet width generally weakens the outlet velocity gradient and changes the momentum exchange at the impeller exit, which leads to a pronounced variation in the generated head. By contrast, the flow rate $\boldsymbol{Q}$ directly controls the operating point of the pump and strongly affects both incidence condition and internal hydraulic loss, so it exhibits a high sensitivity to both Head $\boldsymbol{H}$ and Efficiency $\boldsymbol{\eta}$.

The blade wrap angle $\boldsymbol{\Delta\varphi}$ mainly influences the flow path length and the guidance effect of the blade passage. Its influence is weaker than that of $\boldsymbol{b}$ and $\boldsymbol{Q}$, but it still causes noticeable changes in the pressure rise process and hydraulic loss distribution. The number of impeller blades $\boldsymbol{P}$ affects the blade loading and flow guidance ability, and therefore has a moderate effect on head and a relatively weak effect on Efficiency $\boldsymbol{\eta}$. The blade angle at trailing edge $\boldsymbol{\beta}$ mainly modifies the local flow discharge direction at the blade outlet, so its effect is secondary under the present parameter range. The height of volute diffusion section $\boldsymbol{k}$ shows the lowest sensitivity because, within the investigated range, its variation only slightly changes the downstream diffusion process and has limited influence on the main energy transfer process inside the impeller.

Therefore, the Morris-type screening results indicate that the parameters directly associated with the impeller outlet flow structure and the operating condition dominate the hydraulic response, whereas the parameters related mainly to secondary geometric adjustment exhibit relatively weak influence.

5.2.3 LHS-PRCC Results

In this study, we applied LHS to generate 100 sets of parameter samples from the ranges provided in Table 6 and performed numerical simulations. The resulting parameter samples, along with the calculated head and efficiency values, are presented in Table 10.

Table 10: LHS results.

Number	Number of Impeller Blades	Blade Wrap Angle (°)	Blade Angle at Trailing Edge (°)	Impeller Outlet Width (mm)	Height of Volute Diffusion Section (mm)	Flow Rate (m^3/s)	H (m)	η (%)
1	23	63	24.6	40.9	308.4	0.2133	89.24	81.957
2	29	58	26.8	38.3	309.6	0.2014	100.17	80.787
3	28	66	23.4	48.9	346	0.1767	123.191	78.434
4	26	61	24.2	47.2	335.6	0.2167	100.87	80.422
5	26	59	28.5	47.8	358.1	0.2059	114.142	82.887
6	30	59	29	48.8	346.3	0.2024	99.452	80.656
7	23	55	30.8	44.4	320.7	0.1871	103.164	75.62
8	29	52	25.6	45.9	361.1	0.177	115.537	76.386
9	24	61	26	40.1	297	0.167	97.681	75.226
10	23	67	26.8	39.8	282.7	0.2129	88.479	79.143
11	27	52	24.5	47.3	289.4	0.1875	101.648	81.024
12	31	67	24.1	44.6	352	0.173	96.679	79.479
13	29	66	26.9	45.9	326.2	0.1789	115.114	77.402
14	29	56	24.8	48.6	296.5	0.1945	119.856	76.736
15	29	63	28.4	46.8	330.1	0.1716	117.075	76.104
16	30	54	26.5	45.7	295.6	0.2103	110.386	80.552
17	27	65	29.7	45.8	349.4	0.2047	97.115	81.768

(Continued)

Table 10 (continued)

Number	Number of Impeller Blades	Blade Wrap Angle (°)	Blade Angle at Trailing Edge (°)	Impeller Outlet Width (mm)	Height of Volute Diffusion Section (mm)	Flow Rate (m^3/s)	H (m)	η (%)
18	24	64	28.7	42.4	324.7	0.2025	105.616	78.769
19	30	57	25.5	38.7	318.2	0.1861	94.473	75.188
20	27	52	29.7	44.1	310.3	0.1973	99.088	78.378
21	27	69	29.5	41.1	342.9	0.1948	91.801	81.336
22	26	59	26.1	43.8	316.3	0.1985	90.267	82.44
23	24	67	25.3	49.8	289.2	0.1663	117.582	76.964
24	31	63	28.5	41.4	292.2	0.1852	98.449	79.394
25	30	65	24.1	39	375.7	0.1639	104.76	78.51
26	31	57	27.9	46.8	356.9	0.1904	109.294	75.259
27	26	68	24.8	49.1	373.7	0.1828	105.525	82.85
28	30	66	30.1	38.7	314.1	0.2185	116.693	75.453
29	24	64	31	47.5	370.3	0.1958	97.763	81.717
30	25	65	24.6	42.2	338.4	0.1785	102.673	76.91
31	30	55	28.9	43.8	363	0.1925	108.666	76.867
32	25	57	30.3	38.5	343.3	0.1875	114.155	75.322
33	26	68	27	49.4	322.2	0.1978	98.214	79.079
34	30	67	25.1	49.4	344.1	0.2043	108.009	76.262
35	27	68	30.6	42.8	286.9	0.1933	90.241	82.096
36	24	56	25.7	44.4	283.6	0.1839	113.505	80.599
37	30	60	27.9	46.5	340.9	0.1885	120.197	80.672
38	30	57	23.6	45	323.7	0.199	114.751	81.303
39	29	69	28.4	50.4	338.8	0.1903	120.218	82.973
40	26	62	28	43	281.6	0.209	92.089	78.156
41	25	60	29.9	43.6	299.9	0.1633	101.4	75.971
42	27	60	23.4	42.2	363.8	0.1769	115.107	76.16
43	27	61	29	51.4	341.9	0.2099	109.697	78.828
44	28	59	29.5	39.1	336.9	0.1816	113.085	79.189
45	23	52	26.2	41.5	375	0.1945	97.711	77.019
46	29	65	26.4	39.3	301.6	0.1915	112.825	78.649
47	30	57	24	50.2	296.1	0.1737	110.345	80.477
48	25	58	28.2	50.7	317.5	0.1657	100.563	78.271
49	24	61	23.1	42.7	307	0.2135	101.321	81.241
50	29	54	27.6	40	305	0.217	89.58	79.463
51	24	63	26.7	47.3	329.2	0.1747	100.184	76.319
52	27	56	23.5	44.2	330.5	0.2018	90.416	79.48
53	30	54	29.7	41.2	319	0.1996	111.949	80.883
54	30	52	29.4	45.4	321.1	0.1843	119.71	76.038
55	28	63	29.3	39.3	291.2	0.2119	88.548	80.864
56	27	56	27.5	49	345.5	0.1716	107.086	78.274
57	29	52	28.8	48.3	293.8	0.1872	122.151	75.589
58	28	55	25.9	48.7	298.2	0.2171	113.334	79.981
59	23	53	29.9	51.6	308.9	0.2055	121.542	76.648
60	29	63	26	48.4	334.5	0.2067	99.487	81.737
61	31	66	29.7	51.1	378.6	0.1951	119.085	82.01
62	24	64	30.5	44.1	359.3	0.1892	107.278	78.852
63	26	55	26.1	44.6	378.1	0.1983	88.835	82.075

(Continued)

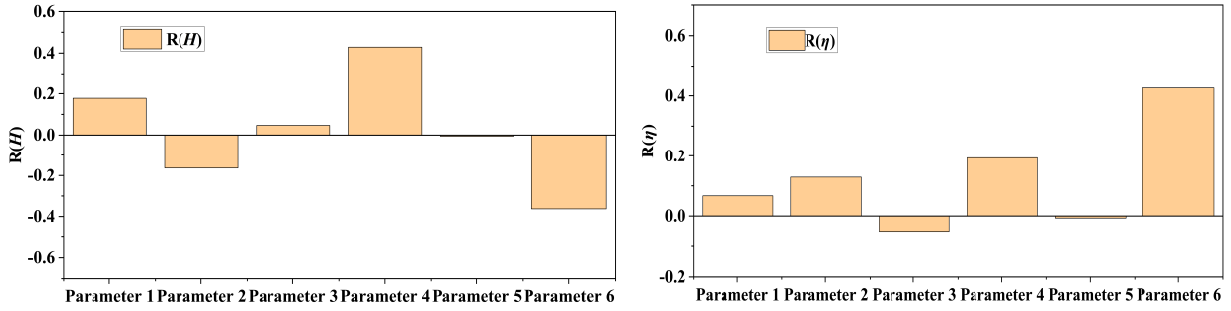
Table 10 (continued)

Number	Number of Impeller Blades	Blade Wrap Angle (°)	Blade Angle at Trailing Edge (°)	Impeller Outlet Width (mm)	Height of Volute Diffusion Section (mm)	Flow Rate (m^3/s)	H (m)	η (%)
64	24	52	27.2	40.7	332	0.1618	104.837	75.226
65	23	54	25.5	43.1	332	0.1812	107.839	77.089
66	30	67	28.7	38.9	316.7	0.2034	89.589	79.134
67	23	53	24	46.3	303.4	0.1662	110.324	79.513
68	28	51	28.2	47.7	282.1	0.1728	123.529	80.04
69	29	66	24.9	42.4	302.5	0.2085	93.055	80.73
70	25	62	28.6	40.6	289.6	0.1767	117.442	80.729
71	25	59	24.7	40.8	348.2	0.1969	112.07	80.233
72	31	62	24.3	38.3	368.9	0.1652	95.794	75.793
73	23	58	30.7	47	312.1	0.2152	119.223	81.963
74	25	61	29.1	41.8	312.3	0.2108	95.687	79.261
75	24	62	23.8	40.3	365.3	0.1861	90.147	77.175
76	29	58	25.3	50.9	284.6	0.2159	112.805	82.675
77	29	58	30.4	49.7	297	0.2129	104.267	82.003
78	28	56	27.7	45.9	293.2	0.1671	105.17	78.872
79	27	67	25.6	39.6	360.6	0.2014	94.755	82.944
80	28	66	26.9	39.8	357.5	0.2145	89.347	81.57
81	26	69	24.2	43.9	290.9	0.2112	102.03	78.338
82	28	65	23.2	44.7	288.2	0.1691	122.845	79.153
83	29	67	23.2	50.7	350.5	0.1795	105.095	81.703
84	26	64	26.7	47.2	315.4	0.2059	89.166	79.836
85	26	59	26.8	50	310.2	0.2028	98.261	75.848
86	27	53	24.2	45.6	325.8	0.1756	117.904	76.811
87	25	53	29.2	47.8	327	0.1712	116.677	82.75
88	25	55	27.4	48.1	371.7	0.1642	120.197	75.957
89	24	59	25.4	48.7	305.9	0.1687	116.423	79.076
90	29	51	25	46	354.3	0.1935	116.392	82.526
91	24	62	30.2	51.3	362.3	0.168	119.307	75.814
92	28	59	24.5	45.2	367.2	0.2003	117.601	76.377
93	28	61	28.3	43.3	325	0.1852	109.85	76.687
94	26	68	25.2	45.7	350.3	0.1623	121.513	75.858
95	31	65	27.3	49.8	355.5	0.1775	120.676	79.322
96	26	65	26.3	41.1	369.5	0.1799	112.587	79.133
97	31	54	31	41.3	351.9	0.2073	107.629	82.592
98	27	52	30.9	40.2	347.7	0.1824	92.01	76.089
99	25	63	23.7	42	375.9	0.1705	115.945	75.317
100	27	64	26.5	46.6	335.9	0.1732	108.248	79.935

Using the Latin hypercube sampling results presented in Table 10, the PRCC values for the six parameters were computed to assess their relationships with both the Head $\boldsymbol{H}$ and Efficiency $\boldsymbol{\eta}$. The relative importance of the parameters was ranked according to the absolute value of the PRCC. The PRCC calculation results of the parameters are shown in Table 11 and Fig. 8.

Table 11: Partial rank correlation coefficient ***R*** of each parameter.

Parameter Number	Parameter	R (***H***)	R (***η***)
1	Number of impeller blades ***P***	0.178	0.0669
2	Blade wrap angle ***Δφ***	−0.1637	0.1291
3	Blade angle at trailing edge ***β***	0.0472	−0.0533
4	Impeller outlet width ***b***	0.4292	0.1937
5	Height of volute diffusion section ***k***	−0.0053	−0.0069
6	Flow rate ***Q***	−0.3629	0.4255



(**a**) Head ***H*** (**b**) Efficiency ***η***

Figure 8: Comparative analysis chart of r results for LHS-PRCC.

The PRCC analysis results indicate that the sensitivity of each parameter to Head ***H*** in descending order is as follows: ***b*** > ***Q*** > ***P*** > ***Δφ*** > ***β*** > ***k***. The sensitivity of each parameter to Efficiency ***η*** in descending order is as follows: ***Q*** > ***b*** > ***Δφ*** > ***P*** > ***β*** > ***k***. The three parameters of the impeller outlet width ***b***, the number of impeller blades ***P*** and the blade angle at trailing edge ***β*** are positively correlated with the Head ***H***, while the three parameters of the blade wrap angle ***Δφ***, the height of volute diffusion section ***k*** and flow rate ***Q*** are negatively correlated with the Head ***H***; The four parameters of the flow rate ***Q***, the blade wrap angle ***Δφ***, the impeller outlet width ***b*** and the number of impeller blades ***P*** are positively correlated with the Efficiency ***η***, while the height of volute diffusion section ***k*** and the blade angle at trailing edge ***β*** is negatively correlated with Efficiency ***η***.

The PRCC results are physically consistent with the Morris-type screening results and further confirm that the dominant factors are mainly associated with the pump operating condition and the impeller outlet geometry. The flow rate ***Q*** is the most sensitive parameter for Efficiency ***η*** because it directly determines the matching relationship between the pump design condition and the actual operating condition. When the flow rate deviates from the optimal operating range, the incidence angle, internal recirculation, separation, and hydraulic loss all increase, which causes an evident variation in Efficiency ***η***. This is why ***Q*** shows the largest positive correlation with Efficiency ***η*** and a strong negative correlation with Head ***H***.

The impeller outlet width ***b*** remains the most influential geometric parameter because it strongly affects the outlet flow capacity, pressure diffusion, and loss generation in the impeller-volute coupling region. A wider or narrower outlet width changes the balance between velocity energy and pressure energy, thus significantly affecting both Head ***H*** and Efficiency ***η***. The blade wrap angle ***Δφ*** also shows non-negligible sensitivity because it alters the blade passage development and the fluid guidance process along the impeller channel. Compared with these parameters, the number of impeller blades ***P*** and the blade angle at trailing edge ***β*** mainly affect the local blade loading and outlet flow direction, so their influence is weaker under the

present operating and geometric ranges. The height of volute diffusion section $\boldsymbol{k}$ still has the smallest PRCC magnitude, indicating that its contribution to the overall hydraulic performance remains limited.

In summary, both the Morris-type screening results and the PRCC results suggest that the hydraulic performance of the studied multistage centrifugal pump is mainly controlled by the operating flow rate and the impeller outlet geometry, while the influence of the volute diffusion-section height is comparatively weak. This consistency also improves the physical interpretability of the obtained sensitivity ranking.

6 Conclusion

This study developed a CFD-based numerical modeling framework integrating hydraulic performance evaluation and sensitivity analysis for the assessment of underground pump station schemes equipped with multistage centrifugal pumps. The proposed framework combines three-dimensional numerical simulation based on the Reynolds-averaged Navier–Stokes approach, the RNG k-ε turbulence model, and global sensitivity analysis methods to quantitatively investigate the relationship between pump configurations, hydraulic performance, and key design parameters. Based on the developed numerical framework, three centrifugal pump schemes, including two single-suction vertical three-stage centrifugal pumps and one double-suction centrifugal pump, were systematically evaluated in terms of structural characteristics and hydraulic performance. The results demonstrate that the single-suction vertical three-stage volute centrifugal pump with conventional flow channels exhibits better overall hydraulic adaptability for the investigated underground pump station under the specified design conditions. Furthermore, the modified Morris screening method and the LHS–PRCC approach were integrated to identify the dominant hydraulic parameters affecting pump head and efficiency. The sensitivity analysis results indicate that only a limited number of parameters have significant effects on the hydraulic performance. The impeller outlet width $\boldsymbol{b}$ is identified as the most influential parameter affecting the pump head $\boldsymbol{H}$, whereas the flow rate $\boldsymbol{Q}$ exhibits the highest sensitivity to efficiency $\boldsymbol{\eta}$. In contrast, the height of the volute diffusion section $\boldsymbol{k}$ has a relatively minor influence on both head and efficiency. The consistent sensitivity rankings obtained from the two methods further demonstrate the reliability of the proposed analysis framework. Overall, the developed CFD-based numerical framework provides a systematic and quantitative methodology for evaluating centrifugal pump schemes and identifying critical hydraulic parameters. It can provide theoretical support for the hydraulic design, performance assessment, and parameter selection of multistage centrifugal pump systems in underground pump stations.

Acknowledgement: None.

Funding Statement: The authors would like to acknowledge the financial support of National Natural Science Foundation of China, grant number 52539006.

Author Contributions: The authors confirm contribution to the paper as follows: Yuan Tang: data curation; formal analysis; methodology; software; validation; visualization; writing—original draft. Tengjiao Guo: conceptualization; investigation; software. Ran Tao: project administration; investigation; resources; supervision; writing—review & editing. Ruofu Xiao: conceptualization; project administration; resources; funding acquisition; methodology; writing-review & editing. All authors reviewed and approved the final version of the manuscript.

Availability of Data and Materials: The data that support the findings of this study are available from the corresponding author, upon reasonable request.

Ethics Approval: Not applicable.

Conflicts of Interest: The authors declare no conflicts of interest.

References

1. Sonawat A, Kim S, Ma SB, Kim SJ, Lee JB, Yu MS, et al. Investigation of unsteady pressure fluctuations and methods for its suppression for a double suction centrifugal pump. Energy. 2022;252(2):124020. doi:10.1016/j.energy.2022.124020.
2. Jiang J, Zhang N, Liu X, Gao B, Cao P. Effect of the staggered impeller on reducing unsteady pressure pulsations of a centrifugal pump. Energy Sci Eng. 2022;10(1):194–207. doi:10.1002/ese3.1022.
3. Wang Z, Qian Z, Lu J, Wu P. Effects of flow rate and rotational speed on pressure fluctuations in a double-suction centrifugal pump. Energy. 2019;170(2):212–27. doi:10.1016/j.energy.2018.12.112.
4. Dehghan AA, Shojaeefard MH. Experimental and numerical optimization of a centrifugal pump volute and its effect on head and hydraulic efficiency at the best efficiency point. Proc Inst Mech Eng Part C J Mech Eng Sci. 2022;236(9):4577–98. doi:10.1177/09544062211056019.
5. Dehghan AA, Shojaeefard MH, Roshanaei M. Exploring a new criterion to determine the onset of cavitation in centrifugal pumps from energy-saving standpoint; experimental and numerical investigation. Energy. 2024;293(2):130681. doi:10.1016/j.energy.2024.130681.
6. Chang H, Wang Z, Peng G, Shi W, Lin R, Zhou L. Role of wall roughness on energy dissipation and Vortex dynamics in self-priming centrifugal pump: a study via entropy generation and Liutex Vortex identification. Energy. 2025;337(4):138733. doi:10.1016/j.energy.2025.138733.
7. Koranteng Osman M, Wang W, Yuan J, Zhao J, Wang Y, Liu J. Flow loss analysis of a two-stage axially split centrifugal pump with double inlet under different channel designs. Proc Inst Mech Eng Part C J Mech Eng Sci. 2019;233(15):5316–28. doi:10.1177/0954406219843573.
8. Qian C, Luo X, Yang C, Wang B. Calculation and verification of balance force of multistage pump balance drum. Proc Inst Mech Eng Part C J Mech Eng Sci. 2022;236(1):153–64. doi:10.1177/09544062211017957.
9. Sakran HK, Aziz MSA, Khor CY. Blade wrap angle impact on centrifugal pump performance: entropy generation and fluid-structure interaction analysis. Comput Model Eng Sci. 2024;140(1):109–37. doi:10.32604/cmes.2024.047245.
10. Zhao Z, Jiang L, Bai L, Pan B, Zhou L. Numerical simulation and entropy production analysis of centrifugal pump with various viscosity. Comput Model Eng Sci. 2024;141(2):1111–36. doi:10.32604/cmes.2024.055399.
11. Salifou Adam A, Mrad H, Marouani H, Fouad Y. Experimental and numerical investigation on high-pressure centrifugal pumps: ultimate pressure formulation, fatigue life assessment and topological optimization of discharge section. Comput Model Eng Sci. 2023;137(3):2845–65. doi:10.32604/cmes.2023.030777.
12. Gonza´lez J´, Ferna´ndez J, Blanco E, Santolaria C. Numerical simulation of the dynamic effects due to impeller-volute interaction in a centrifugal pump. J Fluids Eng. 2002;124(2):348–55. doi:10.1115/1.1457452.
13. Alemi H, Ahmad Nourbakhsh S, Raisee M, Najafi AF. Effects of volute curvature on performance of a low specific-speed centrifugal pump at design and off-design conditions. J Turbomach. 2015;137(4):041009. doi:10.1115/1.4028766.
14. Lettieri C, Defoe J, Spakovszky ZS. An investigation of nonlinear flow oscillations in a high-pressure centrifugal pump. J Turbomach. 2015;137(11):111004. doi:10.1115/1.4031250.
15. Bozorgasareh H, Khalesi J, Jafari M, Gazori HO. Performance improvement of mixed-flow centrifugal pumps with new impeller shrouds: numerical and experimental investigations. Renew Energy. 2021;163:635–48. doi:10.1016/j.renene.2020.08.104.
16. Gu Y, Bian J, Wang Q, Stephen C, Liu B, Cheng L. Energy performance and pressure fluctuation in multi-stage centrifugal pump with floating impellers under various axial oscillation frequencies. Energy. 2024;307(1):132691. doi:10.1016/j.energy.2024.132691.
17. Chang H, Yang J, Wang Z, Peng G, Lin R, Lou Y, et al. Efficiency optimization of energy storage centrifugal pump by using energy balance equation and non-dominated sorting genetic algorithms-II. J Energy Storage. 2025;114(12):115817. doi:10.1016/j.est.2025.115817.
18. Li Z, Dong W, Jiang H. Multi-objective optimization of centrifugal pumps based on extreme learning machine with adaptive non-dominated sorting genetic algorithms III. Phys Fluids. 2025;37(3):037191. doi:10.1063/5.0257717.

19. Wang W, Liu S, Pei J, Sun J, Sun Q. Efficiency improvement and pressure pulsation reduction of volute centrifugal pump through diffuser design optimization. J Energy Storage. 2024;102(01):114184. doi:10.1016/j.est.2024.114184.
20. Wu T, Wu D, Gao S, Song Y, Ren Y, Mou J. Multi-objective optimization and loss analysis of multistage centrifugal pumps. Energy. 2023;284:128638. doi:10.1016/j.energy.2023.128638.
21. Li H, Zhang R, Chen H, Liu Y, Tao F, Fu Q, et al. Effect of single blade trailing edge side fracture on flow characteristics of centrifugal pump. Phys Fluids. 2024;36(10):105127. doi:10.1063/5.0230539.
22. Ionescu-Bujor M, Cacuci DG. A comparative review of sensitivity and uncertainty analysis of large-scale systems—I: deterministic methods. Nucl Sci Eng. 2004;147(3):189–203. doi:10.13182/NSE03-105CR.
23. Cacuci DG, Ionescu-Bujor M. A comparative review of sensitivity and uncertainty analysis of large-scale systems—II: statistical methods. Nucl Sci Eng. 2004;147(3):204–17. doi:10.13182/04-54CR.
24. Yi X, Zou R, Guo H. Global sensitivity analysis of a three-dimensional nutrients-algae dynamic model for a large shallow lake. Ecol Model. 2016;327:74–84. doi:10.1016/j.ecolmodel.2016.01.005.
25. Xu X, Sun C, Huang G, Mohanty BP. Global sensitivity analysis and calibration of parameters for a physically-based agro-hydrological model. Environ Model Softw. 2016;83(8):88–102. doi:10.1016/j.envsoft.2016.05.013.
26. Stübing S, Kreuzfeld G, Müller RP, et al. Initial design and optimization of turbomachinery with CFturbo and optiSLang. In: Proceedings of the WOST-Optimierungs-und Stochastiktage; 2014 Nov 20–21; Weimar, Germany.
27. Chang H, Tang G, Zhou L, Peng G, Shi W, Huang R. Investigation of energy dissipation mechanisms and unsteady flow characteristics of a cooling pump based on sweeping jet inflow. Energy Convers Manag. 2026;351(4):120959. doi:10.1016/j.enconman.2025.120959.
28. Singhal AK, Athavale MM, Li H, Jiang Y. Mathematical basis and validation of the full cavitation model. J Fluids Eng. 2002;124(3):617–24. doi:10.1115/1.1486223.
29. Morris MD. Factorial sampling plans for preliminary computational experiments. Technometrics. 1991;33(2):161–74. doi:10.1080/00401706.1991.10484804.
30. Ge Q, Menendez M. Extending Morris method for qualitative global sensitivity analysis of models with dependent inputs. Reliab Eng Syst Saf. 2017;162(10):28–39. doi:10.1016/j.ress.2017.01.010.
31. McKay MD, Beckman RJ, Conover WJ. A comparison of three methods for selecting values of input variables in the analysis of output from a computer code. Technometrics. 2000;42(1):55–61. doi:10.1080/00401706.2000.10485979.
32. Marino S, Hogue IB, Ray CJ, Kirschner DE. A methodology for performing global uncertainty and sensitivity analysis in systems biology. J Theor Biol. 2008;254(1):178–96. doi:10.1016/j.jtbi.2008.04.011.
33. Helton JC, Davis FJ. Illustration of sampling-based methods for uncertainty and sensitivity analysis. Risk Anal. 2002;22(3):591–622. doi:10.1111/0272-4332.00041.
34. Celik IB, Ghia U, Roache PJ, Freitas CJ. Procedure for estimation and reporting of uncertainty due to discretization in CFD applications. J Fluids Eng Trans ASME. 2008;130(7):078001. doi:10.1115/1.2960953.
35. Oberkampf WL, Roy CJ. Verification and validation in scientific computing. Cambridge, UK: Cambridge University Press; 2010.